

ChemComm

Accepted Manuscript



This is an *Accepted Manuscript*, which has been through the Royal Society of Chemistry peer review process and has been accepted for publication.

Accepted Manuscripts are published online shortly after acceptance, before technical editing, formatting and proof reading. Using this free service, authors can make their results available to the community, in citable form, before we publish the edited article. We will replace this *Accepted Manuscript* with the edited and formatted *Advance Article* as soon as it is available.

You can find more information about *Accepted Manuscripts* in the [Information for Authors](#).

Please note that technical editing may introduce minor changes to the text and/or graphics, which may alter content. The journal's standard [Terms & Conditions](#) and the [Ethical guidelines](#) still apply. In no event shall the Royal Society of Chemistry be held responsible for any errors or omissions in this *Accepted Manuscript* or any consequences arising from the use of any information it contains.

Cite this: DOI: 10.1039/c0xx00000x

www.rsc.org/xxxxxx

ARTICLE TYPE

In situ Monitoring of Li-O₂ Electrochemical Reaction on Nanoporous Gold using Electrochemical AFM

Rui Wen^{a,b} and Hye Ryung Byon^{a*}

Received (in XXX, XXX) XthXXXXXXXXXX 20XX, Accepted Xth XXXXXXXXXXXX 20XX

DOI: 10.1039/b000000x

Lithium-oxygen (Li-O₂) electrochemical reaction on nanoporous gold (NPG) is observed using in situ atomic force microscopy (AFM) imaging coupled with potentiostatic measurement. Dense Li₂O₂ nanoparticles form a film at 2.5 V, which is decomposed at 3.8–4.0 V in ether-based electrolyte.

In recent years, extensive studies have been conducted to improve rechargeable nonaqueous Li-O₂ battery performance. Despite large theoretical energy density (~3 kWh kg⁻¹) accomplished by formation and decomposition of insoluble Li₂O₂ product for discharge and recharge, respectively, parasitic reactions have afflicted the Li-O₂ battery with high cathodic polarization potential and poor cycling performance.¹⁻³ The origins of unintended reactions arise from emergence of superoxide (O₂⁻), as the reduced O₂ form, during discharge^{4,5} and the high potential reached during recharge due to the difficulty of electrochemical decomposition of Li₂O₂ and the presence of side products such as lithium carbonate (Li₂CO₃).⁵ The O₂⁻ is believed to cause considerable degradation of aprotic organic solvents via nucleophilic attack.^{4,5} Accordingly, a highly superoxide-tolerant electrolyte is needed, and ethers and dimethyl sulfoxide (DMSO) have demonstrated their suitability.⁵⁻⁸ In addition, the high recharge potential results in oxidation of electrolyte and carbon cathode.⁹⁻¹¹ Employment of promoters (or catalysts)^{12, 13} and limited depth of discharge¹⁴ have aided in the smooth decomposition of Li₂O₂ at lower recharge potential. Recently, more endeavors have been focused on restriction of the Li₂CO₃ formation. One of the attractive ways is to replace typical carbon cathodes with other conducting electrodes because the carbon oxidation occurring from as low as 3.5 V (referenced to Li⁺/Li) is involved in the formation of Li₂CO₃.^{9-11, 15} Indeed, NPG,^{7, 16} indium tin oxide (ITO)¹⁷ and titanium carbide (TiC)¹⁸ cathodes have exhibited less Li₂CO₃, thus enhancing the cycling performance of Li-O₂ cells albeit with small capacity. In particular, the NPG cathode has been highlighted as demonstrating remarkably low overpotentials for discharge and recharge.^{7, 16} This promising result is predominantly attributed to the unique material properties and interfacial reaction with the O₂ gas. Yet, there has been less detailed study for Li-O₂ electrochemical reaction accommodated on the NPG such as the NPG-O₂ interaction and correlated effects for O₂ reduction and oxidation reaction. Here, we present in situ visual evidence of Li-O₂ products nucleating, growing, and decomposing on the NPG with respect to operating potentials. In situ AFM imaging of NPG

surface is conducted under the Li-O₂ electrochemical reaction in the ether-based electrolyte. The dense Li₂O₂ nanoparticles form a film and eliminate during reduction and oxidation, respectively, with lower overpotentials compared with highly ordered pyrolytic graphite (HOPG) electrode.¹⁹ We suggest that rich active sites having high O₂ adsorption affinity on NPG^{20, 21} is key to determine Li₂O₂ shape and Li-O₂ cell performance.

The NPG was prepared by dealloying of a white gold leaf foil (Ag/Au ≈ 50/50) via acid leaching and annealing under vacuum (see ESI Experimental Section for details), which dissolved Ag and constructed Au ligaments with nanopores. A scanning electron microscopy (SEM) image in **Figure S1a** shows the three-dimensional porous structure of NPG with a size of 30–50 nm for both Au ligaments and nanopores. Elemental mapping with energy dispersive X-ray spectrometry (EDS) depicts homogeneous dispersion of the remaining Ag over the Au ligaments (**Figure S1b–d**).^{22, 23} The atomic % ratio of Ag/Au is around 30/70 attained from X-ray photoelectron spectroscopy (XPS) analysis in **Figure S2**. It is noted that the quantity of remaining Ag on the NPG is higher than the other NPGs reported to be around 5 atomic %.^{22, 23} The as-prepared NPG with a size of 2 × 2 cm² was put on the rigid HOPG substrate and employed as the working electrode in a Li-O₂ model cell. Metallic Li used for counter and reference electrodes was suspended above the NPG electrode and fully immersed in Ar or O₂ gas-saturated tetraethylene glycol dimethyl ether (tetraglyme) (total 0.9 mL, H₂O < 5 ppm) containing 0.5 M of LiTFSI (LiN(SO₂CF₃)₂). All cell assembly and electrochemical measurements coupled with AFM scanning were conducted in an Ar-filled glove box (H₂O < 1 ppm). **Figure 1** shows representative cyclic voltammetry (CV) curves at the potential range of 2.0–4.5 V and a sweep rate of 5 mV s⁻¹. Upon the negative-direction sweep under O₂, onset of the oxygen reduction reaction (ORR) occurs at 2.7–2.8 V and the peak is apparent at 2.3–2.5 V, which are compared with no significant peak under Ar. Onset of the oxygen evolution reaction (OER) occurs during the positive-direction sweep at 3.0 V and with the peak current at 3.2–3.5 V. These ORR and OER are attributed to formation and decomposition of Li₂O₂, respectively (2Li⁺ + O₂(g) + 2e⁻ ↔ Li₂O₂(s)). The onset ORR/OER potentials on the NPG (around 2.7–2.8/3.0 V) are in close proximity to the thermodynamically reversible Li-O₂ potential (E_{rev} = 2.96 V), which are distinguished from those for HOPG (2.5 and over 3 V for ORR and OER, respectively).¹⁹ The overpotentials for the ORR/OER on the NPG are also considerably lower than those on

gold disk,²⁴ HOPG,¹⁹ and glass carbon electrodes.^{6, 24} Representatively, the ORR peak on the NPG is exhibited at 2.3–2.5 V, which is 200–400 mV higher than that on the HOPG.¹⁹ Superior ORR on the NPG arises from its catalytic activity. The ligament curvatures in the NPG are comprised of concentrated atomic steps and kinks,^{20, 21} which accommodate the active sites for the ORR. In addition, a high concentration of Ag on the ligaments can significantly increase O₂ adsorption affinity further.^{18, 19} Two OER peaks having almost identical peak-current to the ORR one are exhibited around 3.27 and 3.5 V in **Figure 1b**, which are unlike the HOPG presenting three OER peaks at 3.37, 3.46 and 3.79 V.¹⁹ Over 3.8 V, a new oxidation peak appears in both Ar and O₂, which is associated with the oxidation of tetraglyme electrolyte^{13, 19} and the redox reaction of the Ag in the NPG ($\text{Ag}^+ + e^- \leftrightarrow \text{Ag}$, $E_{\text{rev}} \approx 0.80$ V vs. SHE (the standard hydrogen electrode)²⁵) with the corresponding reduction peak at around 3.8 V.

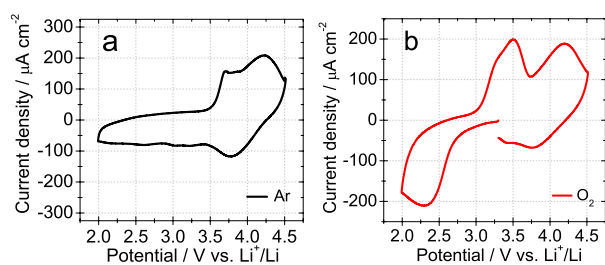


Figure 1. Representative CV curves on NPG electrodes in Li–O₂ model cells with (a) Ar- and (b) O₂-saturated 0.5 M LiTFSI in tetraglyme at a potential range of 2.0–4.5 V and a sweep rate of 5 mV s⁻¹. The NPG electrodes in (a) and (b) were prepared separately, providing different capacitance.

The AFM topography images scanned with the CV sweep at a sweep rate of 5 mV s⁻¹ display in situ formation and decomposition of Li–O₂ product on the NPG. The AFM scanning was conducted for an arbitrarily selected area (2 × 2 μm²) at a rate of 8.5 min per image. **Figure 2** and **Figure S3** shows the NPG surface upon potential-controlled ORR and OER where the AFM scanning direction is denoted by the yellow arrow at the right bottom corner of each image. At the open circuit potential (OCP), the as-prepared NPG surface consists of the ligaments and pores (**Figure 2a**), which are consistent with the SEM image in **Figure S1a**. Along the negative-direction sweep of CV trace to 2.48 V, no notable change on the NPG surface is observed at nanometer scale while at 2.48 V insoluble products emerge (**Figure 2b**). To clarify the dynamic process of the Li–O₂ product formation, we repeatedly obtained the AFM images on the same area whilst holding the potential at 2.48 V (**Figure 2b–d**). The nanoparticle-shaped products gradually grow on the ligaments over time (**Figure 2c**) and cover the NPG ligaments and nanopores (**Figure 2d–e**). The subsequent positive-direction sweep in **Figure 2e–h** shows decreasing particle size after 2.96 V (**Figure 2e**) and apparent elimination of product over 3.8–4.0 V (**Figure 2f**). Such rapid decomposition of the products contributes to the obscure image at 3.45–3.8 V and some drift after just approaching 4.0 V in **Figure 2f**. The ligaments and pores of NPG are exposed without any nanoparticle product when maintaining the potential at 3.8 V for 5 min (**Figure S4**). Over 4.0 V, the bare NPG surface is revealed and either NPG morphology change or newly

deposited product is not significantly observed at nanometer scale (**Figure 2f–h**).

Formation and decomposition of Li₂O₂ as the main Li–O₂ product can be addressed by the XPS. For the XPS analysis, we prepared three NPG electrodes and performed ORR at 2.4 (ORR–2.4V), 2.0 V (ORR–2.0V) and OER at 4.5 V (OER–4.5V), separately, using the potential-controlled mode at a sweeping rate of 1 mV s⁻¹. The cathodes were then washed and dried under vacuum, and directly transferred into the XPS vacuum chamber

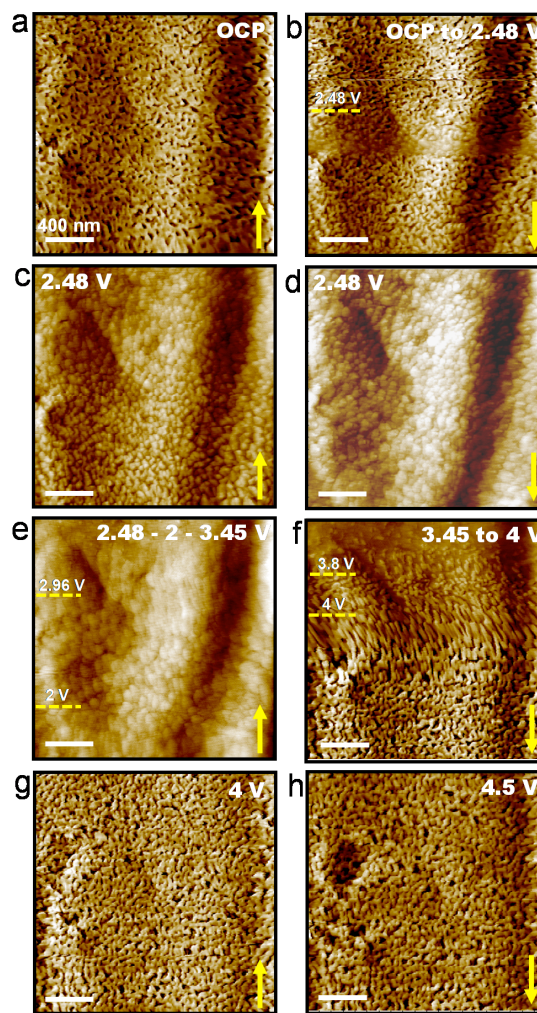


Figure 2. In situ AFM topography images of NPG electrode upon ORR and OER in Li–O₂ model cells with O₂-saturated 0.5 M LiTFSI in tetraglyme. The potentiostatic measurement was carried out at a potential range of 2.0–4.5 V and sweeping rate of 5 mV s⁻¹. Each AFM image was acquired with 8.5 min scan time. (a) OCP, (b–e) ORR at (b) OCP–2.48, (c–d) 2.48, (e) 2.48–2 V, and (e–h) OER at (e) 2–3.45, (f) 3.45–4, (g) 4, (h) 4.5 V. The AFM scanning direction is indicative of the yellow arrows at the right bottom corner of each image. Some potential milestones are also denoted on the left side (b, e, and f). The scale bars are 400 nm. The z-axis scale bars of all images are shown in **Figure S3**.

without air exposure. **Figure 3** shows spectra obtained by synchrotron X-ray with a photon energy of 650 eV. The lower photon energy compared to those from Al and Mg K α sources (1486.5 and 1253.6 eV, respectively) provides a smaller penetration depth and thus information from a thinner layer of the surface. The survey spectra in **Figure 3a** display decrease and increase of Au 4f_{7/2}, 4f_{5/2} (84, 88 eV) and Ag 3d_{5/2}, 3d_{3/2} peaks

(368, 374 eV) upon the ORR and OER, which correspond to deposition and decomposition of Li–O₂ products on the NPG electrodes, respectively. In particular, the disappearance of Au and Ag peaks on the ORR–2.0V reveals the fully covered NPG

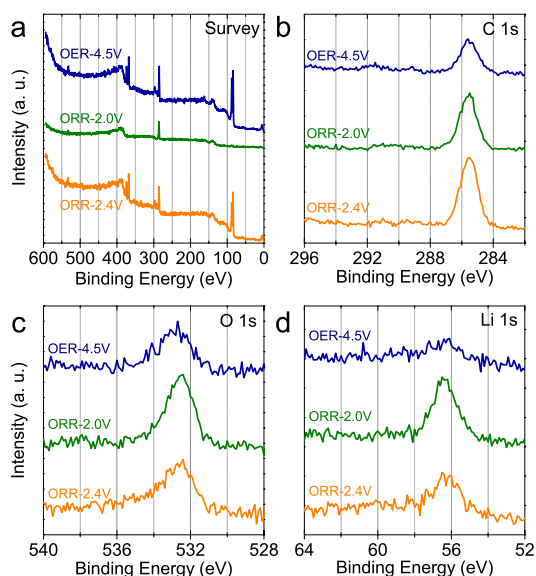


Figure 3. Synchrotron X-ray photoelectron spectra (photon energy \approx 650 eV) of NPG electrodes with different ORR and OER states via potentiostatic control at a sweeping rate of 1 mV s⁻¹. Spectra in (a) survey, (b) C 1s, (c) O 1s and (d) Li 1s BE region with ORR at 2.4 V (ORR–2.4V, bottom orange), 2.0 V (ORR–2.0V, middle green) and OER at 4.5 V (OER–4.5V, top blue).

electrode by the Li–O₂ products, which is consistent with the AFM images during the deep ORR (**Figure 2d–e**). All NPG electrodes show the similar carbon-related peaks (285.5 eV) deconvoluted to sp³ hybridized carbon (285.2 eV) and C–O (286.1 eV)²⁶ in the C 1s binding energy (BE) region (**Figure 3b**), which are indicative of physically adsorbed tetraglyme. The O and Li 1s BE regions in **Figure 3c–d** reveal the main Li–O₂ product of Li₂O₂. The O 1s peak at 532.4 eV and Li 1s peaks at 56.3 eV on the ORR–2.4V and ORR–2.0V correspond to those on the reference Li₂O₂ powder (99% purity) showing 532.5 eV for the O 1s and 55.9 eV for the Li 1s peaks under the same measurement condition (**Figure S5**). The small tails over 533.5 eV in asymmetric O 1s peaks on the ORR electrodes can be attributed to Li₂CO₃ having O and Li 1s peaks of 533.6 and 56.7 eV, respectively (**Figure S5**) whilst its quantity is insignificant. After OER swept up to 4.5 V, the Li₂O₂ is decomposed as evidenced by apparently decreasing Li 1s peak on the OER–4.5V electrode. The C and O 1s BE regions, however, show increasing carboxylate and carbonate peaks (289.1 and 291.6 eV)¹⁵ and still remaining long tail (over 533.5 eV), respectively, on the OER–4.5V, which indicates the oxidation of tetraglyme over 4 V,^{9, 10} thus forming organic carboxylate/carbonate and Li₂CO₃.^{11, 15}

We consider that the Li₂O₂ morphology and its growth process on the NPG are considerably different from those on the HOPG electrode. Upon the HOPG,¹⁹ some of nanoparticle-shaped nuclei formed along the edge of HOPG during initial reduction migrate to the HOPG terrace and gradually increase in the size up to 25 nm (height profile) while most nuclei formed at the edge during later and deeper reduction, close to the reduction peak, swiftly grow to nanoplate shape. The Li₂O₂ nanoplates

formed just above the HOPG surface have large size, such as axial diameter of hundreds of nanometers, length of micrometers and a height of 5 nm, whilst the newly deposited Li₂O₂ nanoplates on the top surface of Li₂O₂ film have much smaller size with the height being maintained at 5 nm. Unlike the HOPG, the Li₂O₂ on the NPG retains the nanoparticle shape for the entire reduction process. In addition, the nanoparticle products do not migrate but grow on a fixed position. Further evidence for the nucleation and growth of Li₂O₂ is displayed in high-magnification AFM deflection images (**Figure 4** and **S6** for 3D image). **Figure 4a** and **4b–f** show the NPG surface at the OCP and time-dependent AFM images at 2.48 V corresponding to **Figure 2b** bottom, **2c** bottom and top, and **2d** top and bottom, respectively (**Figure S3**). At just after approaching 2.48 V, the Li₂O₂ nuclei are formed on the ligaments. We can also observe decreasing NPG pore size (**Figure 4b**), which indicates that the nuclei form along the ligament edge at the initial stage. After the following 5 min, the nanoparticles grow to 30 nm (lateral size) and the resultant Li₂O₂ film covers the NPG surface (**Figure 4c**). This implies that the NPG is attractive to the O₂ adsorption^{20, 21} and Li–O₂ products. The O₂ molecules adsorb on the ligaments with high affinity then stabilize and transform to form Li–O₂ products, either LiO₂ as the intermediate of Li₂O₂ (Li⁺ + O₂(g) + e⁻ → LiO₂) or eventual Li₂O₂ (formed by 2LiO₂ → Li₂O₂ + O₂ or LiO₂ + Li⁺ + e⁻ → Li₂O₂) via charge transfer.²⁷ The strong interaction with the NPG probably leads these Li–O₂ products to adhere to the nucleation sites. In addition, the densely formed nuclei on the copious active sites over the NPG can restrict rapid lateral growth like that observed in the formation of nanoplate shape on the HOPG.¹⁹ Instead, the nuclei gradually increase in size, whilst maintaining the particle shape. Upon further reduction, new nuclei form on this Li₂O₂. In **Figure 4d**, new nuclei of small nanoparticles (arrows) with a lateral dimension of 10 nm can be observed on the Li₂O₂ film, which grow at a growth rate of ca. 4.5 nm min⁻¹ as evidenced by an increasing size of 25 nm in **Figure 4e**. When these nanoparticles are enlarged to a size of 50 nm and create the second film layer, new nuclei appear as indicated by the arrows in **Figure 4f**. These consecutive images exhibit that the nuclei emerge at the edge of the under-layered Li₂O₂ nanoparticles containing abundant steps and kinks.²⁸ The schematic illustration in **Figure 4g** summarizes the sequence of this ORR process. The growth process terminates when the thick Li₂O₂ film hampers the smooth charge transfer.²⁹ The Li₂O₂ film is then eliminated during the OER. Rapid decomposition of the Li₂O₂ at low oxidation potential is revealed by the CV curve (**Figure 1**) corresponding to the AFM images (**Figure 2e–f**). We believe that the NPG–Li₂O₂ interface where the OER occurs¹⁹ is favorable for the electron transfer owing to high electrical conductivity of the NPG whilst further study is needed to understand the OER process.

In summary, we demonstrated in situ ORR and OER process of the Li–O₂ electrochemical reaction on the NPG electrode. The peak potentials for ORR/OER were lower than those on the carbon-based electrodes. The low overpotential of ORR process accounted for the high O₂ adsorption affinity on the NPG, which could allow construction of the dense Li₂O₂ nanoparticle film. The highly conductive NPG with favorable interface with the Li₂O₂ might promote swift decomposition of the Li₂O₂ film

during the OER.

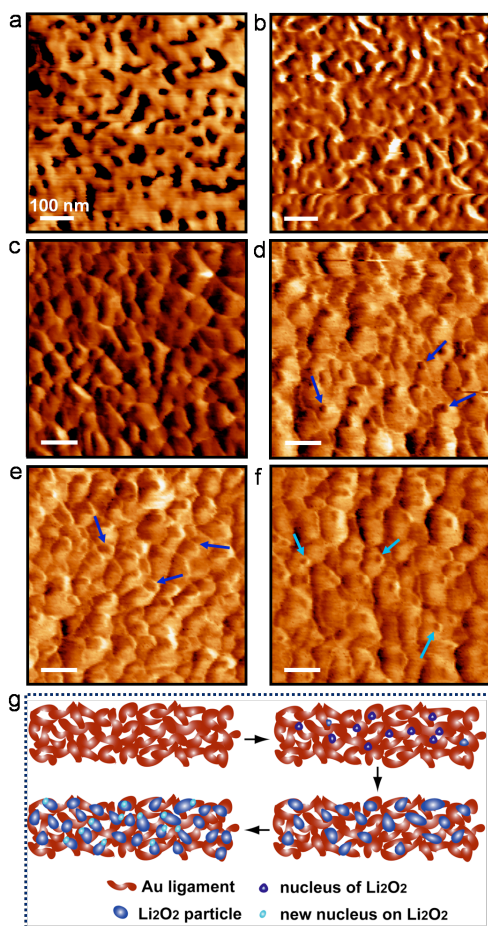


Figure 4. High-magnification AFM images of NPG electrode during ORR and schematic illustration of ORR process. (a–f) Deflection images of NPG at (a) OCP and (b–f) 2.48 V with time-dependent ORR process corresponding to (b) Figure 2b bottom, (c–d) Figure 2c bottom and top, (e–f) Figure 2d top and bottom. The arrows in (d–f) indicate nuclei on the Li₂O₂ film. The scale bars are 100 nm. (g) Schematic illustration of ORR process on NPG.

Acknowledgements

This work was financially supported by RIKEN and JST ALCA program. The XPS experiments using synchrotron radiation were performed at the beamline BL12 of the SAGA Light Source with the approval of the Kyushu Synchrotron Light Research Center (Proposal No. 1310118PT and 1310119R). The authors are thankful to Drs. Hiroyuki Setoyama, Daisuke Yoshimura and Eiichi Kobayashi in SAGA Light Source and Ms. Nadège Bonnet Mercier for XPS operation, and Ms. Misun Hong for EDS element mapping.

Notes and references

^aByon Initiative Research Unit (IRU), RIKEN, Wako-shi, Saitama 351-0198, Japan; E-mail: hrbyon@riken.jp

^bPresent address: Institut für Experimentelle und Angewandte Physik, Universität Kiel, Olshausenstr. 40, 24098 Kiel, Germany

[†] Electronic Supplementary Information (ESI) available: [experimental section, SEM, EDS, XPS and ex-situ AFM images]. See DOI: 10.1039/b000000x/

- G. Girishkumar, B. McCloskey, A. C. Luntz, S. Swanson and W. Wilcke, *J. Phys. Chem. Lett.*, 2010, **1**, 2193-2203.
- P. G. Bruce, S. A. Freunberger, L. J. Hardwick and J.-M. Tarascon, *Nat. Mater.*, 2012, **11**, 19-29.
- Y.-C. Lu, B. M. Gallant, D. G. Kwabi, J. R. Harding, R. R. Mitchell, M. S. Whittingham and Y. Shao-Horn, *Energy Environ. Sci.*, 2013, **6**, 750-768.
- S. A. Freunberger, Y. Chen, Z. Peng, J. M. Griffin, L. J. Hardwick, F. Barde, P. Novak and P. G. Bruce, *J. Am. Chem. Soc.*, 2011, **133**, 8040-8047.
- S. A. Freunberger, Y. Chen, N. E. Drewett, L. J. Hardwick, F. Barde and P. G. Bruce, *Angew. Chem. Int. Ed.*, 2011, **50**, 8609-8613.
- C. O. Laoire, S. Mukerjee, E. J. Plichta, M. A. Hendrickson and K. M. Abraham, *J. Electrochem. Soc.*, 2011, **158**, A302-A308.
- Z. Peng, S. A. Freunberger, Y. Chen and P. G. Bruce, *Science*, 2012, **337**, 563-566.
- M. J. Trahan, S. Mukerjee, E. J. Plichta, M. A. Hendrickson and K. M. Abraham, *J. Electrochem. Soc.*, 2013, **160**, A259-A267.
- B. D. McCloskey, A. Speidel, R. Scheffler, D. C. Miller, V. Viswanathan, J. S. Hummelshøj, J. K. Nørskov and A. C. Luntz, *J. Phys. Chem. Lett.*, 2012, **3**, 997-1001.
- M. M. Ottakam Thotiyl, S. A. Freunberger, Z. Peng and P. G. Bruce, *J. Am. Chem. Soc.*, 2013, **135**, 494-500.
- B. D. McCloskey, A. Valery, A. C. Luntz, S. R. Gowda, G. M. Wallraff, J. M. Garcia, T. Mori and L. E. Krupp, *J. Phys. Chem. Lett.*, 2013, **4**, 2989-2993.
- R. Black, J.-H. Lee, B. Adams, C. A. Mims and L. F. Nazar, *Angew. Chem. Int. Ed.*, 2013, **52**, 392-396.
- E. Yilmaz, C. Yogi, K. Yamanaka, T. Ohta and H. R. Byon, *Nano Lett.*, 2013, **13**, 4679-4684.
- H.-D. Lim, K.-Y. Park, H. Gwon, J. Hong, H. Kim and K. Kang, *Chem. Commun.*, 2012, **48**, 8374-8376.
- D. M. Itkis, D. A. Semenenko, E. Y. Kataev, A. I. Belova, V. S. Neudachina, A. P. Sirotnina, M. Hävecker, D. Teschner, A. Knop-Gericke, P. Dudin, A. Barinov, E. A. Goodilin, Y. Shao-Horn and L. V. Yashina, *Nano Lett.*, 2013, **13**, 4697-4701.
- Y. Chen, S. A. Freunberger, Z. Peng, O. Fontaine and P. G. Bruce, *Nat. Chem.*, 2013, **5**, 489-494.
- F. Li, D.-M. Tang, Y. Chen, D. Golberg, H. Kitaura, T. Zhang, A. Yamada and H. Zhou, *Nano Lett.*, 2013, **13**, 4702-4707.
- M. M. O. Thotiyl, S. A. Freunberger, Z. Peng, Y. Chen, Z. Liu and P. G. Bruce, *Nat. Mater.*, 2013, **12**, 1050-1056.
- R. Wen, M. Hong and H. R. Byon, *J. Am. Chem. Soc.*, 2013, **135**, 10870-10876.
- T. Fujita, P. F. Guan, K. McKenna, X. Y. Lang, A. Hirata, L. Zhang, T. Tokunaga, S. Arai, Y. Yamamoto, N. Tanaka, Y. Ishikawa, N. Asao, Y. Yamamoto, J. Erlebacher and M. W. Chen, *Nat. Mater.*, 2012, **11**.
- L. V. Moskaleva, S. Röhe, A. Wittstock, V. Zielasek, T. Klüner, K. M. Neyman and M. Bäumer, *Phys. Chem. Chem. Phys.*, 2011, **13**, 4529-4539.
- Y. Ding, Y. J. Kim and J. Erlebacher, *Adv. Mater.*, 2004, **16**, 1897-1900.
- L. Zhang, L. Chen, H. Liu, Y. Hou, A. Hirata, T. Fujita and M. Chen, *J. Phys. Chem. C*, 2011, **115**, 19583-19587.
- Y.-C. Lu, H. A. Gasteiger and Y. Shao-Horn, *J. Am. Chem. Soc.*, 2011, **133**, 19048-19051.
- J. A. Dean, *Lange's Chemistry Handbook*, McGraw-Hill Professional Publishing, 1992.
- S. Kundu, Y. Wang, W. Xia and M. Muhler, *J. Phys. Chem. C*, 2008, **112**, 16869-16878.
- Z. Peng, S. A. Freunberger, L. J. Hardwick, Y. Chen, V. Giordani, F. Bardé, P. Novák, D. Graham, J.-M. Tarascon and P. G. Bruce, *Angew. Chem. Int. Ed.*, 2011, **50**, 6351-6355.
- J. S. Hummelshøj, A. C. Luntz and J. K. Nørskov, *J. Chem. Phys.*, 2013, **138**, 034703-034712.
- V. Viswanathan, K. S. Thygesen, J. S. Hummelshøj, J. K. Nørskov, G. Girishkumar, B. D. McCloskey and A. C. Luntz, *J. Chem. Phys.*, 2011, **135**, 214704.